Internal erosion

Pierre-Yves Hicher, Didier Marot, Luc Sibille

Internal Erosion

Pierre-Yves HICHER[+], Didier MAROT[+] and Luc SIBILLE[£]

[+]GeM - Institut de Recherche en Génie Civil et Mécanique, Nantes, France
[£]3SR - Laboratoire sols, solides, structures - risques, Grenoble, France

9.1. Introduction

Internal erosion is one of the main causes of instabilities within hydraulic earth structures such as dams, dikes or levees [FOS 00]. The mechanisms of internal erosion are deeply complex entailing many parameters, a number of which are coupled. In earth structures and within their foundations, two types of internal erosion can be distinguished: suffusion and interface erosion. The suffusion process concerns only the finer particles which, upon being detached, then move into the soil matrix constituted by the coarse particles. Interface erosion can appear within cracks or be caused by concentrated leaks and is then called piping or concentrated leak erosion. When interface erosion appears between two materials with different grain size distributions, it is called contact erosion. This interface, however, relatively large compared to the grain size, can also be located between the soil and the water. In such a case and given a seepage flow normal to the interface, the process is called backward erosion [FEL 07].

9.2. Experimental findings on interface erosion

9.2.1. *Introduction*

Several test devices have appeared in the literature to study the interface erosion of fine-grained soils. The soil samples are subjected to hydraulic stresses by a variety of methods and the interpretations of the experiments are based on a linear erosion law stating that the mass rate of erosion $\dot{m}$, or the volumetric rate of erosion $\dot{\varepsilon}$, is proportional to the excess hydraulic shear stress τ above a threshold value τ_c

which represents the minimal hydraulic shear stress needed to initiate erosion. In equation form, the erosion laws are:

$$\dot{m} = k_{d,m} \left(\tau - \tau_C \right) \quad [9.1]$$

$$\dot{\varepsilon} = k_d \left(\tau - \tau_C \right) \quad [9.2]$$

with $k_{d,m}$ and k_d the erosion rate coefficients so that $k_{d,m} = k_d \, \rho_D$, with ρ_D as the dry soil density.

One of the main devices is the Hole Erosion Test apparatus (HET) developed by Wan and Fell [WAN 04]. The HET can be used in a Proctor mould containing the soil specimen. A 6.35 mm diameter hole is pre-drilled through the centerline-axis to simulate a concentrated leak. A constant hydraulic head or a constant flow rate is applied to the specimen. The data collected during the test consist of the head losses across the sample and the flow rate. When erosion is produced, the resulting increase of the flow rate is used to estimate the increase of the hole diameter and thus to determine the resulting mass rate of erosion.

With the Wan and Fell method [WAN 04] or with the scaling law suggested by Bonelli and Brivois [BON 08], it is possible, thanks to the values of diameter representing the erosion, to determine the value of the erosion rate coefficient and the value of the critical shear stress.

$$I_{HET} = -\log_{10}\left(k_{d,m}\right) \quad [9.3]$$

The erosion development is described by the definition of six groups, varying from extremely slow to extremely rapid.

The submerged Jet Erosion Test (JET) developed by Hanson and Cook [HAN 04] is an apparatus designed to apply a submerged jet on the soil surface which allows *in situ* tests to be performed. The depth of scour beneath the jet is measured over time and, as scour occurs, the hydraulic stress on the soil surface decreases. Hanson and Cook assumed that the equilibrium depth is reached when the stress at the interface is equal to that of the threshold stress. The erosion never ceases, only its speed decreases and the hydraulic shear stress converges asymptotically to the threshold stress. By fitting scour measurements and time data by an asymptotic function, the equilibrium depth and the corresponding critical stress can be deduced. The experimental data are fitted to the calculated scour depth, which provides an estimate of the detachment rate coefficient, k_d.

The soil erodibility classification proposed by Hanson and Simon [HAN 01] is based on both the critical shear stress and the erosion rate coefficient determined by JETs. This classification recognizes five categories from very resistant to very erodible materials.

9.2.2. *Comparative analysis of interface erosion tests*

For the comparison of JET and HET, seven natural fine-grained soils, covering a large range of erodibility were tested [REG 13]. Soils were compacted according to the normal Proctor procedure with an initial water content equal to the optimum water content minus 1%. By using the commonly known methods, the values of the erosion coefficient proved to be systematically higher with the JET than with the HET, and the corresponding mean rate index is systematically smaller with the JET [$I_{JET} = -\log_{10}(k_d)$] than with the HET ($I_{HET}$). The I_{JET}/I_{HET} ratio varies from 0.32 to 0.84. On average, the HET critical shear stress is about fifty times higher than the JET critical shear stress. Moreover, the relative soil classifications provided by the two erodimeters do not exactly match.

9.2.3. *Interpretation by energy method*

The energy equation for the fluid between the entrance and the exit of the system has been written by White [WHI 99] and Marot *et al.* [MAR 11a]:

$$\begin{aligned} \frac{dE}{dt} &= \frac{d}{dt}\iiint_{Mass}\left(e_{\text{int}} + \frac{u^2}{2} + \vec{g}\cdot\vec{z}\right).dM \\ &= \frac{\partial}{\partial t}\iiint_{Volume}\left(e_{\text{int}} + \frac{u^2}{2} + \vec{g}\cdot\vec{z}\right)\rho\, dV + \oiint_{S}\left(e_{\text{int}} + \frac{u^2}{2} + \vec{g}\cdot\vec{z}\right)\rho\,(\vec{U}\cdot\vec{n})\, dS \end{aligned} \qquad [9.4]$$

and:

$$\frac{dE}{dt} = \frac{dE_{Ther}}{dt} + \frac{dW}{dt} \qquad [9.5]$$

with M: fluid mass; V: fluid volume; e_{int}: fluid internal energy; ρ: fluid density; U: fluid velocity; u, v, w: components; g: gravity; z: coordinates; $\vec{n}$: normal vector of external surface oriented from fluid to environment; E_{Ther}: energy exchange between the system and the environment; W: mechanical work between the entrance and the exit of the system.

Four assumptions can be introduced to simplify the equation. The temperature and thus the internal energy (e_{int}) are constant on the volume. The system is adiabatic, only mechanical work (W) takes place between the entrance and the exit of the system. Fourth, a steady state allows the bypassing of the unsteady term of the kinetic energy. As both tests are performed on fine soils, the detached particles should leave the system without re-deposition and the variation of fluid density can be neglected. Hence equations [9.4] and [9.5] become:

$$\frac{dW}{dt} = \frac{\partial}{\partial t} \iiint_{Volume} (\vec{g} \cdot \vec{z})\, \rho \, dV + \oiint_{S} \left(\frac{u^2}{2} + \vec{g} \cdot \vec{z} \right) \rho \, (\vec{U} \cdot \vec{n}) \, dS \qquad [9.6]$$

9.2.3.1. *HET analysis in terms of energy*

The energy equation is applied between the upstream Section A and the downstream Section B of the HET. The apparatus is horizontal, so the term $\vec{g} \cdot \vec{z}$ is null on average. The fluid passes successively through a contraction, a hole and an expansion. The balance of the energy in the system must take into account the energy dissipation in the contraction and expansion which are named singularities. The total energy dissipation is the sum of the energy dissipated by the work of the pressure forces, the viscous work at the control surface and singularities. The viscous work is assumed to cause erosion in the hole and to have a negligible effect on the other parts of the system. So the dissipation of total energy in the system can be written as:

$$\left.\frac{dW}{dt}\right|_{Erosion} + \left.\frac{dW}{dt}\right|_{Singularities} = \oiint_{S} \left(\frac{P}{\rho} + \frac{u^2}{2} \right) \rho \, (\vec{U} \cdot \vec{n}) \, dS \qquad [9.7]$$

It is possible to assume that the mass conservation with a same diameter on the whole length has the same average speed in Sections A and B. Moreover, a test was performed in the HET with a non-erodible polyacrylic model of the specimen with its pre-drilled hole. On a range of flow rates corresponding to the HET range from 0.02 l/s to 0.42 l/s, the percentage of head losses transformed into friction and erosion is roughly 25%. Thus, equation [9.7] becomes:

$$\left.\frac{dW}{dt}\right|_{Erosion} = 0.25 \left(P_A - P_B \right) Q \qquad [9.8]$$

where P_A, P_B are the pressures in Sections A and B, respectively, and Q is the injected flow rate.

9.2.3.2. *JET analysis in terms of energy*

In the case of the JET, the energy equation [9.6] is applied between the nozzle and the escape hatch of the submergence tank. The assumptions of a steady flow in time leads to neglecting the term: $\frac{\partial}{\partial t}\iiint_{Volume}(\vec{g}\cdot\vec{z})\,\rho\,dV$.

In comparison with free jet, the jet which occurs in front of a soil-water interface is subjected to a deviation from the centerline. It is assumed that erosion is mainly associated with this deviation which induces an increase of shear stress and a great variation of pressure. Without any soil-water interface, at the J depth beneath the nozzle, Beltaos and Rajaratnam [BEL 74] expressed the variation of vertical velocity as a function of the lateral distance r from the centerline of the jet by:

$$u(r,J)=\exp\left(-0.693\left(\frac{r}{b_u}\right)^2\right)u(0,J) \qquad [9.9]$$

where b_u is the distance from the centerline corresponding to a decrease of half vertical velocity ($u(b_u, J) = 0.5\ u(0, J)$); $b_u = 0.093\ (J\text{-}J_P)$; J_P is the depth corresponding to the potential core and $u(0, J)$ is the vertical velocity at the center of the jet.

In front of a wall, Beltaos and Rajaratnam [BEL 74] observed that the shear stress of the wall increases linearly with r up to a maximum value obtained for $r = 0.14\ J$. Moreover, when the r/J ratio increases from 0 to 0.14, the wall pressure decreases rapidly, reaching 10% of the maximum value of the stagnation pressure on the jet centerline axis. Thus, at J depth, erosion is assumed to appear in the space defined by the lateral distance from the jet centerline $r \leq 0.14\ J$.

The majority of the work lost at impact is supposed to be transformed into erosion and the energy dissipation occurring inside the jet itself is neglected. The assumptions of a hydrostatic pressure in the downstream tank and a negligible fluid velocity outside of the jet at impact complete the set of equations.

The temporal derivative of the mechanical work by erosion can be expressed by:

$$\begin{aligned}\left.\frac{dW}{dt}\right|_{Erosion} &= 2\pi\int_0^{0.14\,J}\frac{u^2}{2}\,\rho\,(\vec{U}\cdot\vec{n})\,r\,dr \\ &= \pi\,\rho\,u(0,J)^3\int_0^{0.14J}\left[\exp\left(-0.693\left(\frac{r}{b_u}\right)^2\right)\right]^3 r\,dr\end{aligned} \qquad [9.10]$$

For $J < J_P$, $u(0,J) = u(0,0)$, with $u(0,0)$: initial velocity at the jet origin. For $J > J_P$, $u(0,J)$ is determined by the ratio $u(0,0)\ J_P/J$ proposed by Hanson and Cook [HAN 04].

9.2.3.3. *HET and JET analysis by energy method and erodibility classification*

The energy dissipated by erosion ($E_{erosion}$) is computed by integrating the erosion work over the test duration for both devices. Values of the eroded dry mass are computed by the eroded wet mass/$(1 + w_i)$ ratio, where w_i is the initial water content.

An erosion resistance index is proposed as:

$$I_\alpha = -\log_{10}\left(\frac{Eroded\ dry\ mass}{E_{erosion}}\right) \qquad [9.11]$$

Using the energy analysis, Marot *et al.* [MAR 11a] built an identical soil classification with the two devices and six categories of soil erodibility from very resistant to very erodible (see Figure 9.1)

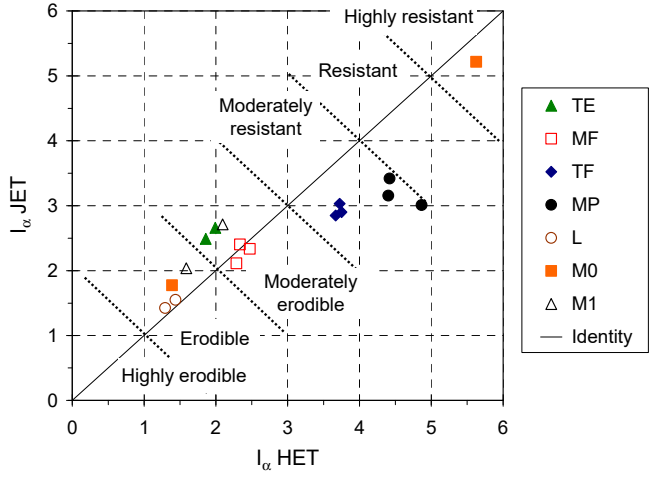

Figure 9.1. *Erosion resistance index determined with JET versus erosion resistance index determined with HET and soil erodibility classification. For a color version of the figure, see www.iste.co.uk/millet/advances.zip*

9.2.4. *Statistical analysis*

A Jet Erosion Test device was used by Regazzoni and Marot [REG 11] in order to characterize the erosion susceptibility of 12 fine soils covering a large part of the

Atterberg limits. The tested samples were compacted with the standard Proctor procedure at optimum water content minus 1%. Several physical parameters were determined and a statistical analysis was performed to identify the main parameters for a correlation with an erosion resistance index (computed by equation [9.11]).

By differentiating dispersive and non-dispersive behaviors, the multivariate statistical analysis leads to an expression of the erosion resistance index as a function of three physical parameters: compaction, saturation ratio and the difference between the clay water content and the liquid limit. These parameters take into account the influence of each phase and the influence of soil plasticity. It is thus possible to reduce the number of variables to describe the erosion susceptibility.

It has been shown that for the soil named M0, a water content discrepancy of 4% is sufficient to induce a variation of soil erodibility from highly resistant to erodible. Thus, the use of a predictive equation for real structure needs to consider the soil heterogeneities and the composition of the pore and the eroding fluid.

9.3. Experimental findings on suffusion

9.3.1. *A mechanics-based understanding of suffusion*

The complex phenomenon of suffusion can be understood as the process by which the finest soil particles become detached and then transported within the porous network constituted by the soil itself. However, a fraction of the detached particles can re-settle or be filtered with the bulk of the porous network. This process can eventually induce local clogging. Detachment, transport and filtration of fine particles are thus inseparable processes. It is worth noting that suffusion is conditioned by the evolving and interdependent characteristics of the fluid phase as well as of the solid phase. Therefore, suffusion depends not only on the geometry of the porous medium but also on the physicochemical characteristics of the medium and of the interstitial fluid.

According to Garner and Fannin [GAR 10] three factors affect the initiation of internal erosion processes: the sensitivity of the material, the condition of critical stress and the critical hydraulic load. In the same manner, Fell and Fry [FEL 13] also distinguished three criteria: (i) the size of the fine soil particles must be smaller than the size of the constrictions between the coarser particles, which form the basic skeleton of the soil; (ii) the amount of fine soil particles must be less than enough to fill the voids of the basic skeleton formed by the coarser particles; and (iii) the velocity of flow through the soil matrix must be high enough to move the loose fine soil particles through the constrictions between the larger soil particles.

It is recognized that suffusion may cause changes in porosity and can also lead to important modifications in the hydraulic and mechanical characteristics of the soil [CHA 11, KE 12, MAR 09, MOF 11b]. Moreover, modifications of the porous medium can be the catalyst for slope instability at the scale of hydraulic embankments [FRY 12]. Although the development of suffusion may be difficult to detect *in situ,* it has to be carefully considered since it can lead to a second phase of erosion, characterized by a blowout and an a significant washing away of fine particles, which induces both a large settlement of the specimen and a relatively strong increase in hydraulic conductivity [SIB 15a]. Thus, to ensure the safety assessment of hydraulic earth structures, suffusion susceptibility must be characterized.

9.3.2. *General principle of laboratory suffusion test apparatus*

For characterizing the initiation and development of suffusion, most experimental devices comprise a rigid wall cylinder [KEN 85, MOF 06, SAI 11, SKE 94, WAN 08,]. The rigid wall is usually made of a transparent tube so that the specimen can be observed visually as it becomes unstable during the erosion process (see Figure 9.2).

a) b)

Figure 9.2. *Downward progression of localized blowout induced by suffusion a) Moffat and Fannin [MOF 06]; b) Sail et al. [SAI 11]*

For the study of suffusion under complex stress states and so as to minimize probable side wall leakage, Bendahmane *et al.* [BEN 08], Marot *et al.* [MAR 09, MAR 11b] and, more recently, Chang and Zhang [CHA 11] developed a specific triaxial cell (see Figure 9.3). This testing device comprises a modified triaxial cell designed to saturate the sample in the upward direction, to consolidate it under

isotropic confinement and finally to force the fluid to percolate throughout the sample in a downward direction. The cell base has a vertical funnel-shaped draining system, specially designed to avoid clogging.

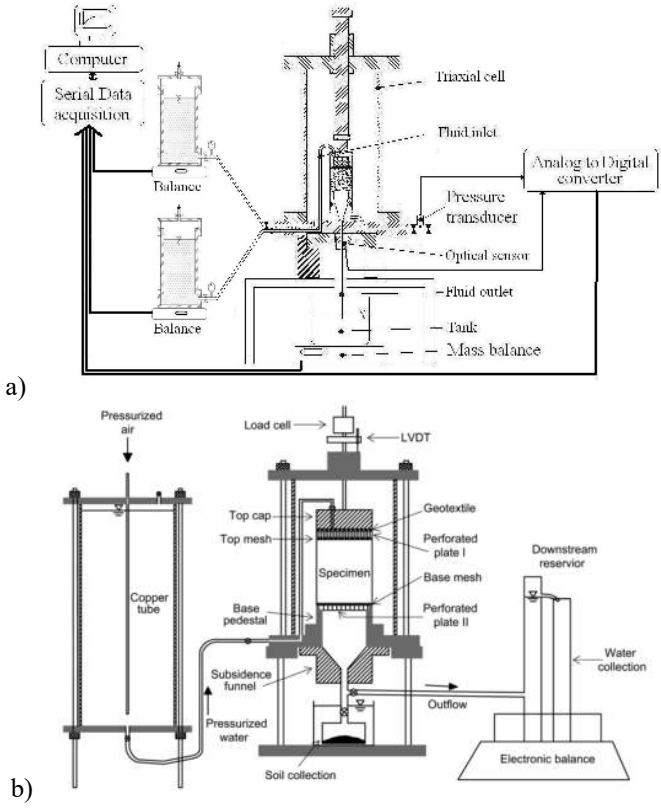

Figure 9.3. *Schematic representation of the apparatus developed by a) Bendahmane et al. [BEN 08]; b) Chang and Zhang [CHA 11]*

With the objective of reproducing full scale stress states, Marot *et al.* [MAR 12a] placed a suffusion test device in the IFSTTAR centrifuge swinging basket. The device comprises a rigid wall cylinder cell and the physical modelling with centrifuge makes it possible to reproduce *in situ* stresses in a small scale model.

In the case of downward seepage flow, three types of filter were used: a porous stone [RED 00] (see Figure 9.4(a)), a drainage layer composed by coarse-grained [KEN 85, WAN 08] (see Figure 9.4(b)) or a wire mesh screen [BEN 08, CHA 11, MAR 09, MAR 11b, MAR 12a, MAR 12b, MOF 06, MOF 11a]. The filter pore

opening size is an important parameter for qualifying the erosion rate [MAR 09]. To take into account this effect, Sail *et al.* [SAI 11] placed a stainless steel mesh screen on the specimen support. This 15 mm thick mesh screen is equipped with a 10 mm pore opening size allowing all the grains of the tested specimens to migrate and with a rim, different wire meshes can be fixed on the mesh screen, allowing only the finer fraction to escape.

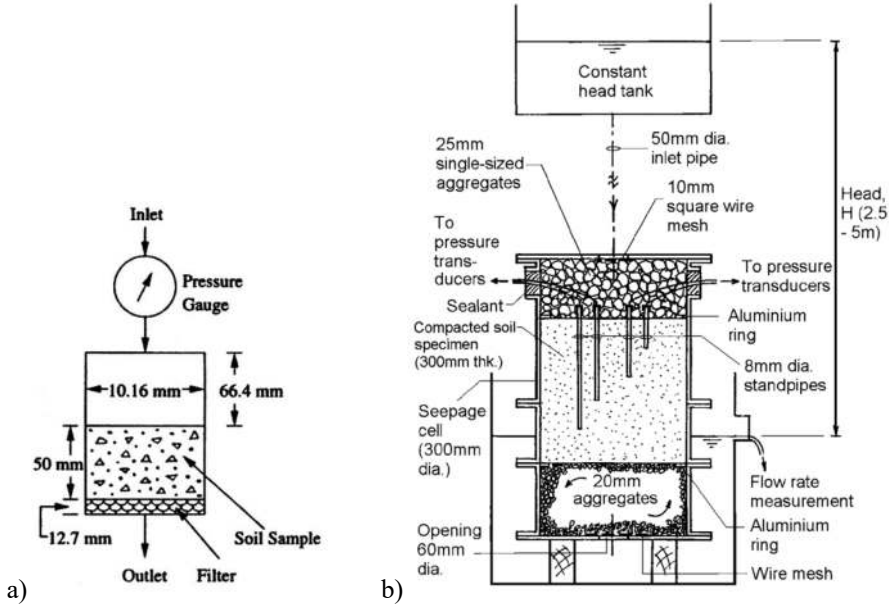

Figure 9.4. *Schematic representation of the apparatus developed by a) Reddi et al. [RED 00]; b) Wan and Fell [WAN 08]*

During suffusion tests, the pore pressure can vary significantly. The pore pressure can be measured by piezometers with visual determination [SKE 94] or be connected to pressure transducers [WAN 08] (see Figure 9.4(b)). Moffat and Fannin [MOF 06, MON 11a] used several total pressure transducers and differential pressure transducers; all connected to pressure ports (see Figure 9.2(a)). To avoid a discrepancy between two pressure transducers, pressure ports can be connected to a multiplex unit which is connected to a single pressure sensor [SAI 11].

To measure the spatial change of density, a gamma densitometric bench was developed by Sail *et al.* [SAI 11]. It comprises a radioactive gamma-ray source and a scintillation counter on the opposite cell side. These components are bonded to a carriage moving in the vertical direction thanks to an endless screw and a controlled electric motor. The position of the carriage is measured by a position transducer.

According to a previous gauging data, a density calculator counts the scintillometer impulses and calculates the mean density of the specimen part located 25 mm around the scintillation counter focal axis.

One of the main difficulties in interpreting suffusion tests is related to detecting the initiation of suffusion. Three approaches have been published in the literature. Skempton and Brogan [SKE 94] suggested relating the onset of internal instability to an increase of hydraulic conductivity. Perzlmaier [PER 07] observed that using the local hydraulic gradient improved the precision of detecting the onset of instability and Moffat *et al.* [MOF 11b] defined the occurrence of internal instability by the decrease with time in local hydraulic gradient. The third approach is based on effluent turbidity [BEN 08, MAR 09, MAR 11b, MAR 12a, RED 00, WAN 08]. Using a turbidimeter allows measuring the effluent turbidity. However, this type of device requires an upward or horizontal flow possibly generating the sedimentation of fine grains between the sample exit and the turbidimeter, which may, in turn, distort the measurements. Marot *et al.* [MAR 11b] suggested a multichannel optical sensor capable of measuring the erosion rate of clay particles or cohesionless fine particles continuously with a downward flow direction. This sensor is composed of four Light Emitting Diodes and four associated Light Dependent Resistors allowing the fluid transparency to be measured. Given the small dimensions of the device, it can be placed close to the particles exiting from the specimen. The optical sensor is thus able to measure instantaneously a large range of clay or silt concentrations in the effluent, without a significant influence of the flow rate. The presence of sand grains in the fluid flow can also be detected.

9.3.3. *Parametric studies*

Three main gradation curves can be distinguished [LAF 89]: a linear distribution, a discontinuous distribution and an upwardly concave distribution. In the case of the discontinuous distribution, a series of intermediary-size grains is missing. The concave distribution consists of a poorly graded coarser fraction associated with a highly graded fine fraction. In this type of soil, the volume between the grains of the coarser fraction is higher than the volume of fine particles, thus enabling the fine particles to migrate. The soils that are likely to suffer from suffusion are, according to Fell and Fry [FEL 07] “internally unstable,” that is their grain-size distribution curve is either discontinuous or upwardly concave. Not much research has been done on the influence of the grain shape; however, according to Voivret [VOI 08] the shape of the grains is an intrinsic characteristic of granular media which could significantly affect their mechanical behavior. By using a triaxial erodimeter,

Marot *et al.* [MAR 12b] determined the suffusion sensitivity of three mixtures of kaolin-aggregates (mixtures with 10% of kaolin). Results have clearly demonstrated that the suffusion process depends on the grain angularity of the coarse fraction. With a same grain size distribution, the angularity of the coarse fraction grains contributes to increasing suffusion resistance.

For the same granular distribution, the modification of the effective stress can induce grain rearrangements. Several tests performed in oedometric conditions on unstable soils showed that a rise in the effective stress causes an increase of the soil resistance to suffusion [MOF 06]. Similarly, when tests were carried out under isotropic confinement [BEN 08], the increase in the confinement pressure led to a decrease in the suffusion rate. On the other hand, for a given initial porosity, Chang and Zhang [CHA 11] showed that the increase of the deviatoric stress is linked to an increase of the maximum erosion rate.

9.3.4. *Characterizing suffusion susceptibility*

Given the complexity of the subject, a preliminary study can be made to evaluate the potential suffusion susceptibility by considering only the grain size distribution. Based on the results, several criteria have been proposed. However, it is worth pointing out that grain size distribution criteria have not taken into account several important parameters such as: the mineralogy of the material, the shape of the grains, the soil density and the effective stress. Finally, even if the transport of particles is geometrically feasible, the action of the hydraulic flow must be sufficient for soil particles to be detached.

In literature, several soil sensibility classifications have been suggested for interface erosion [HAN 01, MAR 11a, WAN 04], whereas erodibility classification for suffusion has not been well established.

In order to characterize soil susceptibility to suffusion, Nguyen *et al.* [NGU 12] compared different interpretative methods. By using a triaxial erodimeter, tests on clayey sand (the tested material is a mixture of 75% sand, percentage by weight, and 25% clay) were performed involving seepage in a downward flow under either hydraulic gradient-controlled or flow rate-controlled conditions. The analysis of flow-rate-controlled tests shows that even if no eroded clay was detected in the effluent, hydraulic conductivity decreased and the hydraulic gradient increased. Under a high hydraulic gradient or under flow rate-controlled conditions, clay

suffusion leads to sand and clay erosion which induces a significant decrease of the specimen volume. According to all the measurements, it appears that the erosion of clayey sand is a consequence of clay suffusion.

The comparison of the hydraulic gradient-controlled tests with the flow rate-controlled tests underlines the different amplitudes of the hydraulic gradient and associated test duration to produce sand erosion. Thus, the history of the hydraulic loading seems to influence clay as well as clayey sand erosion.

For different values of the hydraulic gradient, a matching order of magnitude of clay erosion rate could be measured. Thus, a value of the hydraulic gradient allows neither the initiation and development of clay suffusion nor the initiation of clayey sand erosion to be estimated.

In the case of cohesive soils, Reddi *et al.* [RED 00] suggested representing the porous medium by a system of parallel capillary tubes, each of a constant radius r, which can be estimated by:

$$r = \sqrt{\frac{8\,K}{n}} \qquad [9.12]$$

where n is the porosity, K is the intrinsic permeability: $K = k\ \eta/\gamma_w$, where k is the hydraulic conductivity, η is the dynamic viscosity and γ_w is the specific weight of water.

By this approach, therefore, the hydraulic shear stress along a horizontal capillary tubes system can be expressed by:

$$\tau = \left(\frac{\Delta P}{\Delta L}\right)\frac{r}{2} = \left(\frac{\Delta P}{\Delta L}\right)\sqrt{\frac{2K}{n}} \qquad [9.13]$$

where $\Delta P = P_A - P_B$ is the pressure drop between the upstream Section A and the downstream Section B of the specimen, and ΔL is the distance between Sections A and B. It is worth noting that in equation [9.13], the pressure gradient and permeability have both been considered. Figure 9.5 (a) and (b) show the values of the erosion rate of clay versus the hydraulic shear stress computed by equation [9.13].

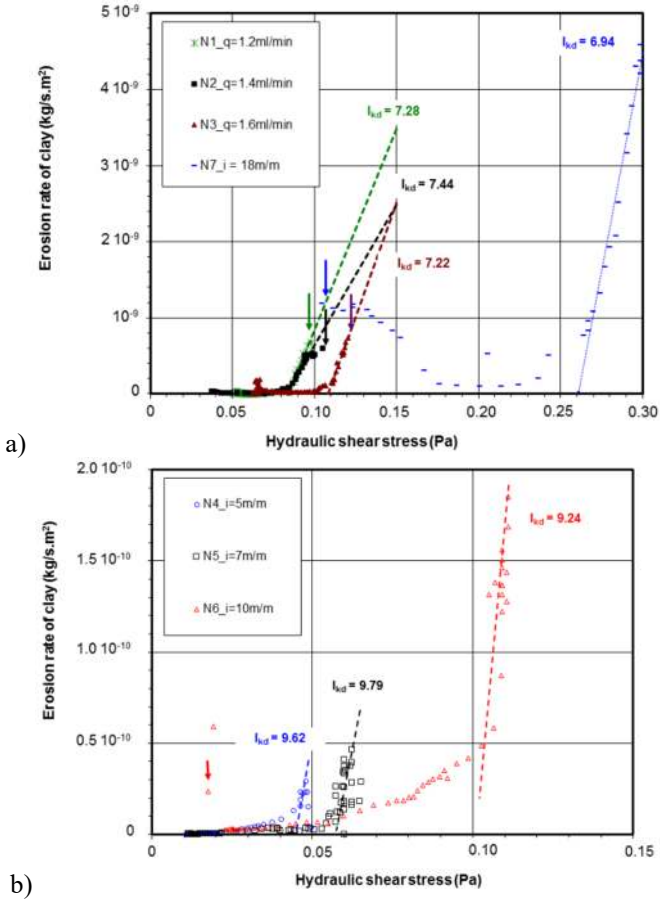

Figure 9.5. *Erosion rate of clay versus hydraulic shear stress. Arrows show time detection of sand grains in effluent: a) flow rate-controlled tests and high hydraulic gradient-controlled test, b) hydraulic gradient-controlled tests. For a color version of the figure, see www.iste.co.uk/millet/advances.zip*

By selecting certain values, a linear correlation between the erosion rate of clay and the hydraulic shear stress can be established. The slope of correlation corresponds to the k_d coefficient. The values of the erosion rate index, I_{kd}, ranged from 6.9 (test N7, see Figure 9.5(a)) to 9.8 (test N5, see Figure 9.5(b)). Linear extrapolation of the obtained correlations allows determining the values of the critical shear stress, which range from 0.02 Pa (test N6, see arrow in Figure 9.5(b)) to 0.12 Pa (test N3, see Figure 9.5(a)).

These results highlight the necessity of taking into account the history of the hydraulic loading, on one hand, and, on the other hand, the evolution of the corresponding specimen response.

The energy conservation equation (equation [9.6]) expresses the total flow power as the summation of the power transferred from the fluid to the solid particles and the power dissipated by the viscous stresses in the bulk. Since the transfer appears negligible in the case of suffusion [SIB 15b], the authors suggest characterizing the fluid loading from the total flow power, P_{flow} expressed by:

$$P_{flow} = (\gamma_w \, \Delta z + \Delta P) Q \qquad [9.14]$$

where $\Delta z = z_A - z_B$, z_A and z_A are the vertical coordinates of Sections A and B, respectively, and Q is the fluid flow rate. $\Delta z > 0$ if the flow is downward, $\Delta z < 0$ if the flow is upward and the erosion power is equal to $Q \, \Delta P$ if the flow is horizontal.

To characterize independently the hydraulic loading and the induced erosion, the energy dissipation is computed by the temporal integration of the flow power for the duration of the test, and the cumulative eroded dry mass is determined. The erosion resistance index is computed by equation [9.11] and the obtained values during the entire test duration are plotted in Figure 9.6.

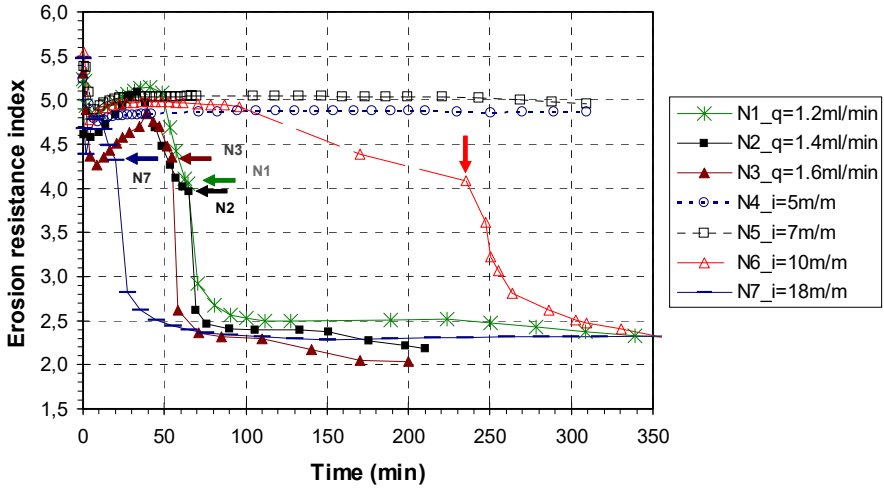

Figure 9.6. *Erosion resistance index versus time. Arrows show time detection of sand grains in effluent. For a color version of the figure, see www.iste.co.uk/millet/advances.zip*

During the suffusion process, the erosion resistance index reached a maximum value within a few minutes from 4.8 (test N7) to 5.2 (test N1). For tests N4 and N5, the erosion resistance index stayed constant during the remaining time of the test at around 4.9 and 5, respectively. For tests N1, N2, N3, N6 and N7, the detection of sand grains in the effluent was associated with a value of erosion resistance index between 4 (test N2) and 4.3 (test N7). The development of sand erosion induced a decrease of the erosion resistance index which led to an asymptote value ranging from 2 (test N3) to 2.3 (tests N1, N6 and N7).

Thus for the tested soil, clay suffusion was characterized by an erosion resistance index at about 5, the initiation of the sand and clay erosion was associated with an average value of the erosion resistance index at about 4.1 and, just before the failure of the specimen, the erosion resistance index was about 2.1. According to these results, the erosion resistance index is identical for hydraulic gradient-controlled tests and for flow rate-controlled tests. These results demonstrate that this approach is efficient in characterizing clay suffusion development and also the induced clayey sand erosion.

9.4. A description of internal erosion based on flow power

In this section the internal erosion of soils, based on the power expanded by the water seepage, is described by numerical experiments carried out with a coupled DEM-LBM model. The discrete element method is used to describe the motion of each grain of the soil, and the dynamics of the interstitial flow is solved with the lattice Boltzmann method [LOM 13]. First, the case of hole erosion is modeled. Then, the expression obtained from these numerical experiments is applied to a case of erosion by suffusion characterized by laboratory tests on glass bead mixtures. Since eroded particles may be filtered in the case of suffusion, unlike in the hole erosion case, the description is completed to take into account this significant feature.

9.4.1. *Detachment of solid particles / initiation of erosion*

9.4.1.1. *A micro hydro-mechanical model of hole erosion*

Numerical experiments of hole erosion were performed with a coupled DEM-LBM numerical method. The bi-dimensional model is displayed in Figure 9.7(a) [LOM 13]. It consists of a tube filled, in its central part, with circular and cohesive solid grains, characterized by a mean diameter d_{mean}. The grains along the tube axis were manually removed in order to create an initial hole with an aperture $d_h \approx 4\ d_{mean}$. The contacts generated in the initial configuration between two grains, or between a grain and a wall of the tube, are cohesive. Normal and shear cohesions,

C_n and C_s, are defined in Figure 9.7(b), and are chosen so that $C_n = C_s = C$. The cohesion is brittle, hence, if cohesion breaks down, the contacts become purely frictional (see Figure 9.7(b)). Finally, any new contact created during the simulation is itself purely frictional.

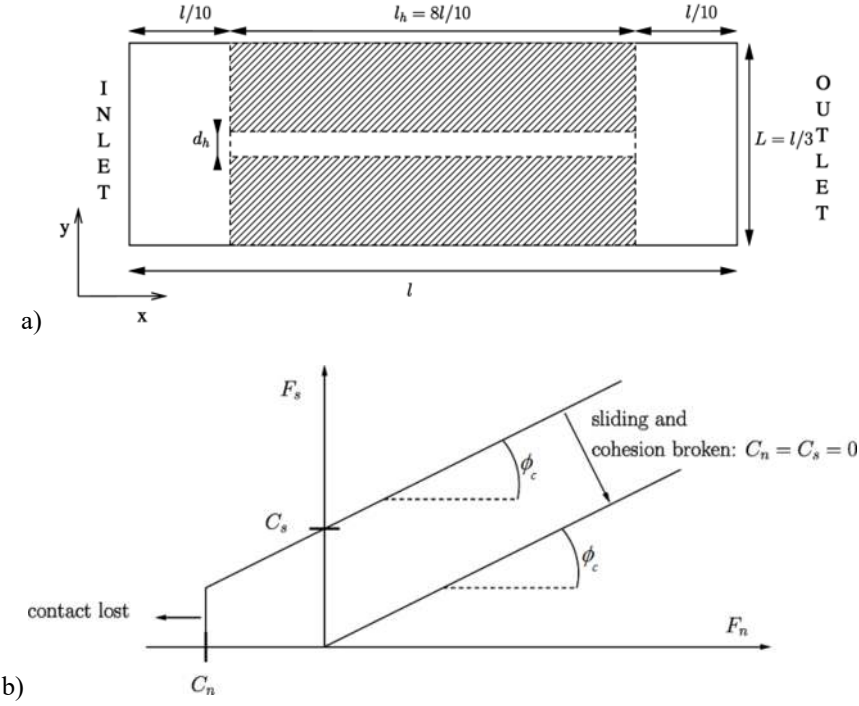

Figure 9.7. *a) Sketch of the numerical model of hole erosion. Hatched regions correspond to the locations of the cohesive granular assembly so that an initial horizontal hole is formed; b) failure criterion of the cohesive brittle contacts*

The tube walls are impermeable with respect to the fluid and constitute a rigid boundary for the solid particles. A pressure drop ΔP is imposed between the inlet and the outlet of the tube to expel the fluid flow through the hole, with a Reynolds number from 0.50 to 40.0. The effect of gravity was excluded in these simulations. These simulations reproducing about 200 s of physical time, and including 800 solid grains and more that 300,000 fluid nodes, were performed for 10 different values of pressure drop, and 7 values of contact cohesion.

Under the action of the fluid flow, solid grains are detached from the boundary of the hole and carried with the fluid to the outlet section of the tube (Figure 9.8(a)).

The grains crossing over this section are considered to be eroded. M_e denotes the cumulated mass of eroded grains and typical time series of M_e are presented in Figure 9.8(b).

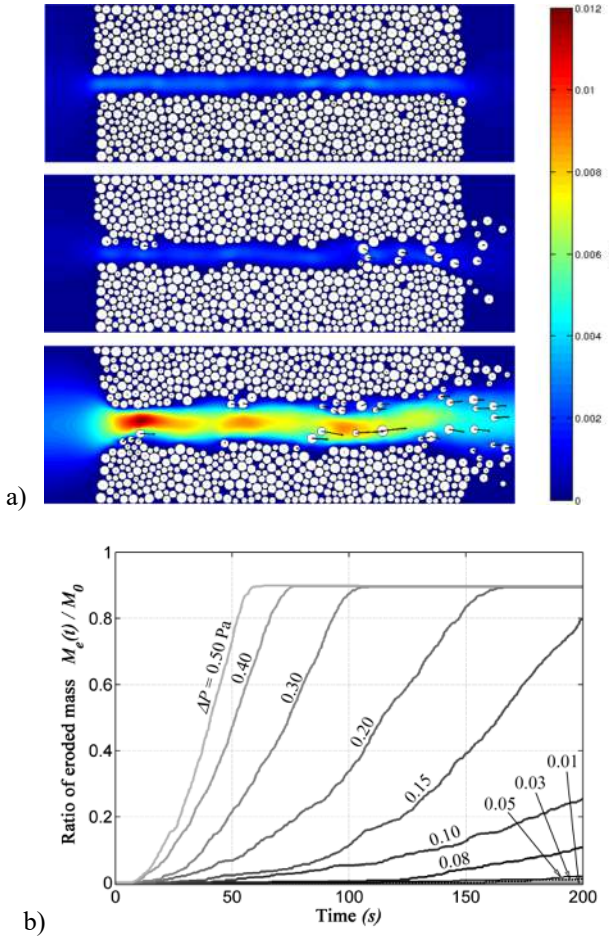

Figure 9.8. *a) Snapshots of a simulation of erosion (at t = 0.7, 13.3 and 55.0 s), the color scale is related to the fluid velocity whereas the translation velocity of solid particles is represented with arrows; b) eroded mass for a given cohesion (C/d = 0.506 N/m) simulated for pressure drops ranging from ΔP = 0.01 to 0.50 Pa. For a color version of the figure, see www.iste.co.uk/millet/advances.zip*

9.4.1.2. *Particle detachment and hydraulic shear stress*

A classical description of the hole erosion (or concentrated leak erosion) consists of representing the hydraulic loading by the hydraulic shear stress τ_s developing on the solid/fluid interface forming the wall of the hole. The erosion rate per unit surface $\dot{\epsilon}$ depends thus on the excess shear stress with respect to the critical stress τ_c below which particles cannot be detached:

$$\dot{\epsilon} = k_d(\tau_s - \tau_c) \qquad \text{if } \tau_s > \tau_c$$

where k_d is an erosion coefficient fixing the kinetics of particle detachment for shear stresses exceeding the threshold.

It is worth noting that a description of such particle detachment driven by the hydraulic shear stress has also been considered in the case of erosion by suffusion by Bonelli and Marot [BON 11], who represented the soil pores as small tubes. They thus assumed solid particles to be detached from the peripheral surface of the tubes as in a piping erosion problem.

Results obtained from the numerical model and presented in Figure 9.9 are in agreement with this interpretation. A parametric study with respect to the contact cohesion C showed that critical stress for particle detachment increases with C, apparently linearly; whereas the erosion coefficient k_d seems independent of C [SIB 15b]. However, these conclusions should be confirmed by further studies involving a wider range of variation of C values.

9.4.1.3. *Particle detachment and fluid flow power*

Characterizing the transport of sediments in river beds by flow or stream power has been suggested by Bagnold [BAG 56, BAG 80] and, more recently, in the case of overland flow sediment transport [FER 98, GOV 92, LOW 89]. In both river and overland flow cases, stream power is defined as the product of the hydraulic shear stress on the bed soil and the mean flow velocity, which provides an estimate of the power dissipated by viscous shear in the fluid near the fluid/solid interface. Bagnold [BAG 80] and Govers [GOV 92] showed that the sediment transport rate can be expressed as a power function of the stream power. Recently, Marot *et al.* [MAR 12a] and Regazzoni and Marot [REG 13] suggested that the internal erosion in soils could be prompted by the power dissipated by the fluid seepage throughout the porous solid phase. Therefore, this section examines the possibility of interpreting the internal erosion of soils from the energetic terms representative of the water flow through the soil.

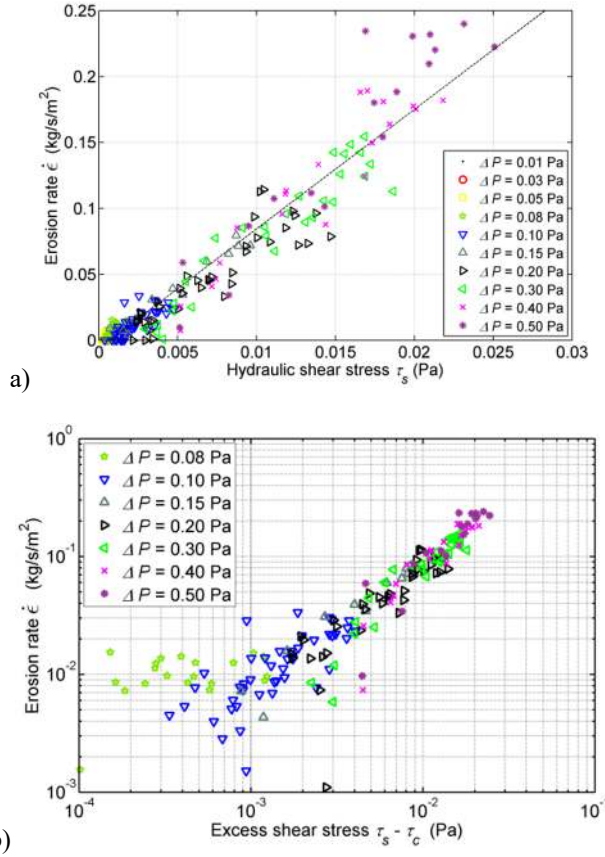

Figure 9.9. *Simulated erosion rate for a cohesion C/d = 0.506 N/m in terms of the hydraulic shear stress estimated on hole boundaries, a) linear scale and b) logarithmic scale (in the latter the excess shear stress $\tau_s - \tau_c$ is used instead of the shear stress and points with shear stress values lower than the threshold τ_c have been removed). For a color version of the figure, see www.iste.co.uk/millet/advances.zip*

It is generally accepted that internal erosion in soils comprises three steps: detachment of solid particles from the initial granular skeleton, their transport within the interstitial space and a possible deposition (or filtration) of the transported particles in soil pores. In the framework of sediment transport in rivers and overland flow, there is no filtration step, and the above interpretation in terms of stream power aims only to characterize the detachment and transport of particles. Consequently, the initial analysis carried out here in the framework of internal erosion is intentionally limited to the steps of detachment and transport. The discrete numerical model has been designed for this purpose to avoid deposition or filtration,

because even if some particles may temporarily settle, the detachment and transport are far more predominant, leading to an irreversible increase of the width of the hole.

9.4.1.3.1. Fluid power of seepage through a granular medium

Let us consider an incompressible viscous fluid. At a position $\vec{x}$ of its volume V, the fluid density ρ, the static pressure p and velocity $\vec{v}$, and the tensor of viscous stresses $\boldsymbol{\sigma}^v$ are defined. The energy conservation equation of a volume V of fluid seeping through solid grains in a tube (Figure 9.10) delimited by inlet and outlet surfaces, S_i and S_o, can be written, disregarding the gravity [SIB 15b]:

$$-\int_{S_i+S_o} p\,\vec{v}\cdot\vec{n}\,dS=\int_{S_G}\left[p\,\vec{v}\cdot\vec{n}_G-\left(\boldsymbol{\sigma}^v\cdot\vec{n}_G\right)\cdot\vec{v}\right]dS+\int_V \sigma_{ij}^v\,\frac{\partial v_i}{\partial x_j}\,dV \qquad [9.15]$$

with $\vec{n}$ the outer unit normal vector to inlet and outlet surfaces, and $\vec{n}_G$ the outer unit normal vector to the boundary surface S_G of solid grains.

The left-hand side of equation [9.15] represents the power supplied to the fluid to flow within the granular assembly. This term is called the flow power P_F. The integral over surface S_G, that will be denoted I_G, represents the power transferred from the fluid to the solid particles, and the remaining volume integral is the power dissipated by viscous stresses in the bulk P_V. Hence, $P_F = I_G + P_V$

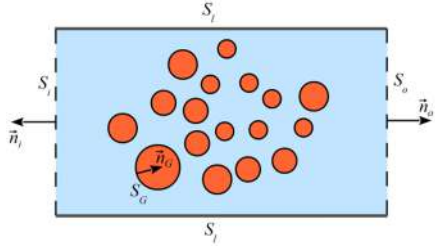

Figure 9.10. *Water seepage through a granular assembly enclosed in a tube: the boundaries of the fluid domain comprised outer boundaries (inlet and outlet sections S_i and S_o, and lateral tube surface S_l) and inner boundaries S_G formed by the solid grains*

It could be of interest to describe the action of the interstitial fluid flow on the solid phase of the soil from the term I_G. However, from a study on laboratory tests of suffusion and hole erosion, it seems difficult to estimate the proportion of the flow power transferred to the solid phase causing its deformation and the detachment of particles, because this transfer represents a quasi-negligible fraction in the case of

suffusion and is highly variable in cases of hole erosion [SIB 15b]. Consequently, attention was paid to the flow power P_F which can be easily estimated, in an engineering context, from a flux and a pressure drop. In addition, the flow power is mainly dissipated by viscosity (P_V) at the vicinity of solid interfaces constituted by the solid grains included in the intact granular skeleton and the detached grains currently transported by the fluid, at least for the seepage configurations under study (see Figure 9.11). Hence, the flow power P_F can be seen as an indicator of the fluid-solid interactions.

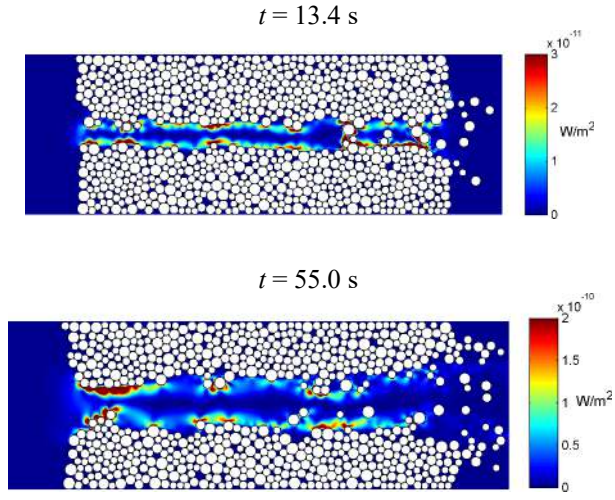

Figure 9.11. *Field of density of power dissipated by viscosity (cohesion C/d = 1.27 N/m and pressure drop ΔP = 0.30 Pa). For a color version of the figure, see www.iste.co.uk/millet/advances.zip*

9.4.1.3.2. Description of particle detachment from the flow power

In the framework of the lattice Boltzmann method, the fluid boundary nodes (FB nodes) were here defined as the computational nodes of the fluid domain constituting the boundary of the latter on the fluid/solid interface. Hence, the power dissipated by viscosity at the FB node, P_V^{FB}, represents the power dissipation occurring most closely with the solid particles. The plotting of the erosion rate in terms of P_V^{FB} in Figure 9.12(a) shows that the erosion rate varies as a power function of the excess power dissipated by viscosity in the direct vicinity of solid particles:

$$\dot{m} \propto \left(P_V^{FB} - P_V^{FB*}\right)^{\beta_V} \qquad [9.16]$$

where P_V^{FB}* is a threshold power below which no particles are detached.

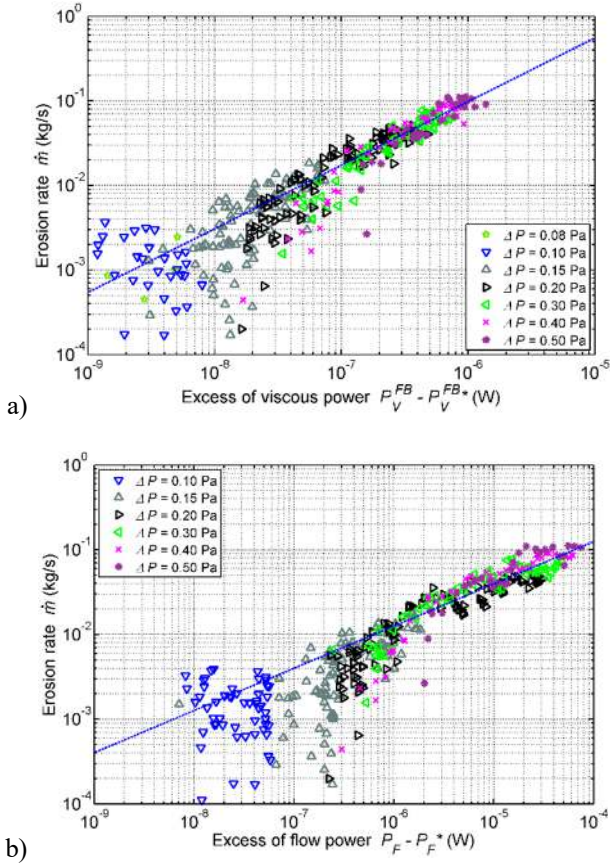

Figure 9.12. *a) Erosion rate as a function of the power dissipated by viscosity at fluid boundary nodes P_V^{FB} (for a cohesionC/d = 1.27 N/m), the dashed line represents an approximation with a power law; b) similar interpretation but in terms of the flow power P_F. For a color version of the figure, see www.iste.co.uk/millet/advances.zip*

P_V^{FB} cannot be directly quantified from a practical point of view. Therefore, an identical interpretation can be made by considering the total flow power P_F, as displayed in Figure 9.12(b). Although the scaling of the erosion rate with P_F is slightly less satisfying than with P_V^{FB} , the erosion rate can also be well expressed by:

$$\dot{m} \propto \left(P_F - P_F*\right)^{\beta_F} \qquad [9.17]$$

where P_F* constitutes a threshold value for particle detachment.

In this last case, the hydraulic loading represented by the flow power P_F, computed as the product between the fluid flux and the pressure drop, is quite easy to determine.

9.4.2. *Description of internal erosion including a filtration step*

We assume here that the description of particle detachment based on the flow power, presented in the previous sections, holds true in the case of erosion by suffusion of granular materials [BON 11]. The mechanisms of the detachment of particles involved in suffusion are assumed to be similar to the one represented with the numerical model of hole erosion. Nevertheless, suffusion may be accompanied by an additional step of filtration, possibly dominating the step of particle detachment, and limiting the erosion of particles after a given time.

Suffusion tests on glass bead mixtures were performed by Sibille *et al.* [SIB 15a] with the oedo-permeameter described in section 9.3.2 [SAI 11]. Bi-disperse glass bead assemblies including 40% of fines were subjected to a downward water flow under a controlled hydraulic gradient *i,* increasing by steps. The tests consisted of successive steps of about 60 min (except for test N6) with a constant hydraulic gradient *i*. The tests presented in Table 9.1 differed from each other by the size of the increment of the hydraulic gradient between each step and the length of the tested samples.

Test	Initial samplelength (mm)	Successive increments of global hydraulic gradient	Duration of hydraulicloadingincrements (h)
N1	250	1-2-3-3.2	1-1-1-1
N2	450	1-2-3-4-4.8	1-1-1-1-1
N3	450	1-2-3-3.7-4.7	1-1-1-1-1
N4	600	1-2-3-4.9-5.5	1-1-1-1-1
N5	250	0.1-0.2-0.4-0.8-1-2.2-3	1-1-1-1-1-1-1
N6	250	0.1-0.2-0.4-0.8-1	1-1-5-4-1

Table 9.1. *Properties of suffusion tests on glass bead assemblies*

Beads transported with the effluent to the outlet of the cell were collected using a sampling device. Time series of the cumulative mass of collected beads are shown in Figure 9.13. Steps of the hydraulic gradient are visible, since the mass increases rapidly at the beginning of each step and tends to stabilize at the end of the step. The decrease of the erosion rate during a hydraulic step is related to the limitation of detachable fine beads. This limitation is dependent on the hydraulic gradient [BON 11], and the possible development of filtration. Consequently, it is assumed that only the erosion rate at the initiation of each step of the hydraulic gradient characterizes particle detachment.

The erosion rate per unit volume, $\dot{\overline{m}}$, is plotted according to the flow power per unit volume, $\overline{P}_F$, for the six tests (N1 to N6) in Figure 9.14. The highest erosion rates displayed in the latter plot correspond to the initiation of increments of the hydraulic gradient and are assumed to be representative of the detachment of solid particles, independently of the quantity of potentially erodible beads and of a possible filtration. This is represented by the upper limit envelope of data plotted with the dashed line in Figure 9.14 and approximated, as suggested in equation [9.17], with the power law:

$$\dot{\overline{m}}^{\text{upper limit}} = \alpha_{\text{ref}} \left(\overline{P}_F\right)^{\beta_F} \qquad [9.18]$$

With $\alpha_{\text{ref}} = 0.003$ and $\beta_F = 0.8$, which can be seen as intrinsic parameters to the tested material and representing its erodability. The threshold flow power $P_F{}^*$ is very low for this kind of material and has been neglected here for the sake of simplicity.

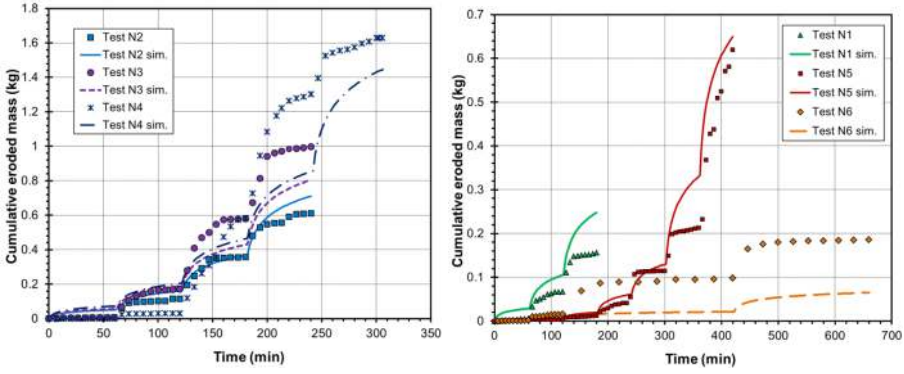

Figure 9.13. *Cumulative eroded mass produced from suffusion tests on glass bead mixtures; symbols represent experimental data whereas continuous lines represent a model prediction. For a color version of the figure, see www.iste.co.uk/millet/advances.zip*

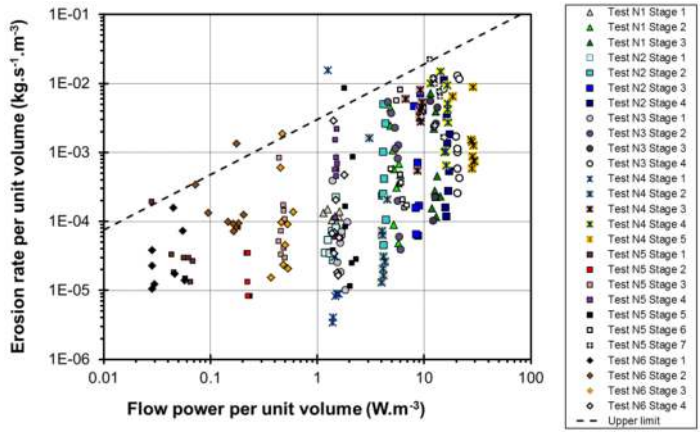

Figure 9.14. *Identification of the maximum erosion rate per unit volume as a function of the flow power per unit volume. For a color version of the figure, see www.iste.co.uk/millet/advances.zip*

The decrease in the erosion rate during each step of the hydraulic gradient emphasizes the necessity of taking into account the history of the hydraulic loading, that is, the amplitude but also the duration of each increment. A history parameter is thus defined, the cumulated flow energy per unit volume $\Delta\overline{E}$ equal to the time integration of the instantaneous flow power $\overline{P}_F$, from the initiation of the considered increment of hydraulic gradient. With this history parameter in mind, the following expression of the mass erosion rate can be suggested [SIB 15a]:

$$\dot{\overline{m}} = \alpha_{\text{ref}} \frac{1}{\dfrac{\Delta\overline{E}}{\overline{P}_F\, t^*} + 1} \left(\overline{P}_F\right)^{\beta_F} \qquad [9.19]$$

where t^*, taken here to equal 130 s, is a characteristic time relative to the material.

For the tests discussed here, the hydraulic conductivity of the material was only slightly affected by erosion. Consequently, by assuming the hydraulic conductivity to be constant and equal to k_0, the one initially measured on the glass bead assembly, the erosion rate per unit volume $\dot{\overline{m}}$, can be computed at any time. The cumulative eroded mass is directly deduced from the latter, integrated over time and compared with the experimental data in Figure 9.13. The suggested description is able to capture the main features of the erosion process. However, the prediction of the eroded mass does not totally agree with the experimental data. Although tests N2

and N3 have been performed with the same parameters (see Table 9.1) and thus stand for the repeatability of the tests, the cumulative mass of particles collected is about 25% larger for test N2 rather than N3. Obviously, the model is not able to describe such a difference since the input parameters are identical, at least almost identical, with an initial hydraulic conductivity k_0 = 1.24 10^{-4} m/s for N2, whereas k_0 = 1.50 10^{-4} m/s for test N3. Consequently, due to the discrepancies within the experimental data, the predictive capacity of the model cannot be absolutely ascertained.

Nevertheless, it is worth noting that this model is rather simple, involving four parameters (α_{ref}, β_F, t^*, k_0) identifiable from a single suffusion test performed by increasing the hydraulic gradient in steps.

9.5. Numerical approaches to describing internal erosion effects in soils

Only a fully coupled hydro-mechanical model can properly provide an exhaustive accurate estimation of internal erosion phenomena. The studies [HIC 13, SCH 10] undertaken here do not claim to describe all the complexities of the problem but to underline the potential role played by particle removal on the macroscopic response of a granular assembly. Simplified approaches have been developed here in order to imitate particle removal due to internal erosion, by exploiting a discrete element model (DEM) and a micromechanical model based on a homogenization technique.

9.5.1. *DEM approach*

9.5.1.1. *Numerical model and kinetics of erosion*

The 3D numerical sample is a granular assembly composed of 10,000 spheres with an initial grading, as presented in Figure 9.15(a). The inter-granular interactions are modeled by a linear elastic relationship between forces and relative displacements, associated with a slip Coulomb model in the tangential contact direction. The “virgin” state sample response to a drained triaxial compression is typically dilative, as shown in Figure 9.16(a) and (c).

Particle removal in the DEM model is based on two assumptions [SCH 10]. First, it can be usefully assumed that seepage flow affects predominantly the less constrained particles of the assembly. Second, particles should be small enough to be transported throughout the pore network. The less loaded particles belonging to the smallest particle fraction are thus the most likely to be eroded. The loading of

each particle p is estimated through its mean internal moment $m^p = \mathrm{tr}\left(\mathbf{M}^p\right)$, where $\mathbf{M}^p$ is the internal moment tensor of the particle p, as defined by Moreau [MOR 97], giving a good representation of the stress state at the particle scale:

$$M_{ij}^p = \sum_{\alpha \in p} r_i^\alpha \, f_i^\alpha \qquad [9.20]$$

where $\vec{r}^{\,\alpha}$ is the vector connecting the center of particle p to the contact point α associated with the contact force $\vec{f}^{\,\alpha}$.

Particles are removed in a repetitive way from the assembly so that they have the smallest m^p value among the 5% smallest particles, consequently limiting the extraction to the finest particles (i.e. only particles $\leq d_5$ are potentially extracted). After the total extraction of fines, the grading curve is changed into the dashed one presented in Figure 9.15(a).

During particle extraction, boundary wall positions are controlled in order to keep the prescribed stresses constant. Extraction is driven so that an equilibrium is reached before any subsequent particle is removed. Between two particle extractions, the system evolves around a quasi-static equilibrium with bursts of kinetic energy whose intensity is linked to the role of the removed particle on the overall stability, possibly resulting in macroscopic deformations. If the extraction process is pursued until the complete removal of the fraction $\leq d_5$ the grading curve of the soil becomes modified, as displayed in Figure 9.15(a).

Particle removals are initiated from different stress ratios $\eta = q/p$ reached along a drained triaxial compression. Simulation results are represented in terms of the eroded fraction *fe*, defined as the ratio of the cumulative mass of removed particles to the initial sample mass, or in terms of the axial strain ε_1.

9.5.1.2. *Sample response to particle extraction*

Figures 9.15(b) and (c) present the volumetric strain of the sample while particles are extracted. During the first stage of the extraction process, the sample exhibits at first no significant volumetric changes whatever the value of η at initiation. Then, two distinct behaviors can be observed. First, for low η values ($\eta \leq 0.72$), contractancy occurs with particle removal and the sample reaches a final equilibrium state after the entire extraction process (5% of solid mass removed). On the other hand, for $\eta \geq 0.72$, there is a transition from a contractant to a dilatant behavior which is associated with a loss of stability in the sample. Indeed, dilatancy occurs for a constant extracted mass value (Figure 9.15(c)), indicating that no new equilibrium state has been reached. It is remarkable that the limiting threshold for

the sample to fail corresponds to the residual state (≈ 0.72) obtained for large shear deformations of the intact specimen, the so-called critical state, as shown in Figure 9.15(d).

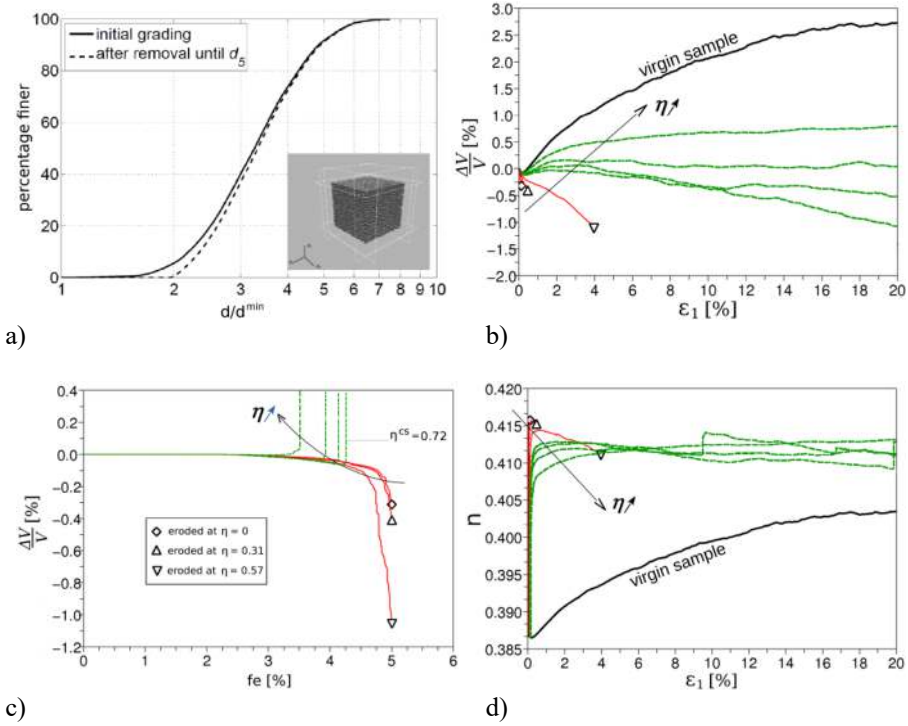

Figure 9.15. *a) Particle size distributions of the DEM numerical sample before and after particle extractions; b)–c) Volumetric strain and porosity, n, change induced by particle removals under different values of the stress ratio $\eta = q/p$. The solid red lines indicate the extraction processes leading to stable configurations after the entire 5% mass extraction (located with symbols), whereas the dash green lines indicate the extraction processes leading to sample failure. The curves labeled "virgin sample" represent the response of the initial sample to the drained triaxial compression*

As shown in Figure 9.15(d), the extraction process tends to increase the porosity regardless of the induced dilative or, more surprisingly, contractive behavior of the sample. Due to the marginal role of removed particles on the overall stability of the assembly, the initial microstructure supports an increase of its porosity with limited rearrangements. This result tends to confirm the results obtained by Muir Wood *et al.* [MUI 10] in 2D: the creation of a more open microstructure due to particle removal dominating the effect of sample compression induced by local destabilizations. The evolution of the porosity appears, for this soil gradation,

therefore, as a pertinent parameter for characterizing materials subjected to erosion, with a measurable overview of induced internal structural changes.

In order to bring all the specimens to failure, triaxial compressions have been pursued for the samples which stabilize after the entire extraction process (Figure 9.16). Intuitively speaking, the increase of the initial porosity produces a change in the specimen from a dilative to a contractive behavior, confirming therefore the importance of monitoring the porosity when considering mechanical properties of a potentially erodible material. Remarkably, the change of the porosity value for the critical state (Figure 9.16(c)) is probably related to the change of the grading induced by particle removal.

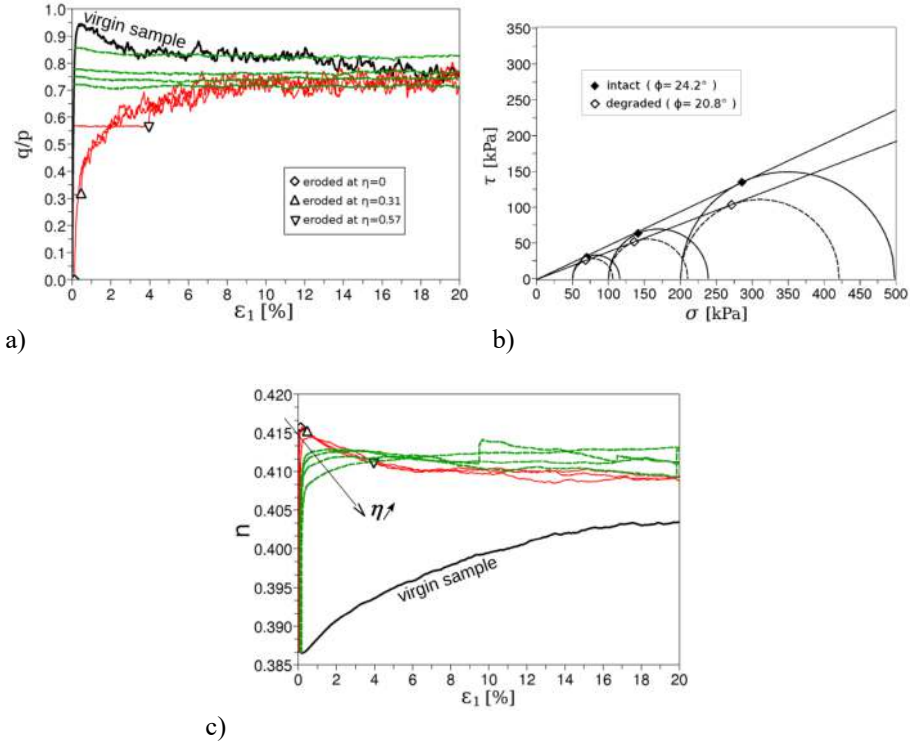

Figure 9.16. *(Left) thick black lines represent the response of the initial dense granular sample to the drained triaxial compression. The three white symbols (for η = 0; 0.31; 0.57) represent the states reached after the particle removal process in the case where particle removal has not led the sample to failure. Thin lines after the symbols represent the response of the "eroded" sample when triaxial compression is pursued. Dashed thin lines represent the path followed during the particle removal process in the case of sample failure during this process. For a color version of the figure, see www.iste.co.uk/millet/advances.zip*

The Mohr-Coulomb limit conditions obtained for both intact and degraded specimens are plotted in Figure 9.16(b). The shear strength of the material has been affected by the removal of some of its constitutive particles, decreasing the internal friction angle from 24.2° for the intact material, to 20.8° for the degraded one which, in this case, corresponds to its residual value. All these modifications in the mechanical properties (internal friction angle, volumetric strain and residual state) of the granular assembly are independent of the initial stress state at which particle extractions are conducted. This would mean that degradation of the mechanical properties does not depend on the mobilized strength in different locations of a soil mass where erosion occurs, but depends only on the erosion progress status.

9.5.2. Micromechanical approach

9.5.2.1. *Stress-strain model*

The numerical approach is based on the use of a homogenization technique for deriving the stress-strain relationship of the granular assembly from forces and displacements at the particle level. The microstructural model developed by Chang and Hicher [CHA 05] treats a soil as a collection of non-cohesive particles. The deformation of a representative volume of the material is generated by mobilizing particle contacts along various orientations. The inter-particle behavior is based on an elastoplastic relationship between local forces and displacements. The elastic part can be estimated from Hertz-Mindlin's formulation, whereas the plastic part is based on a Coulomb criterion with a hardening function of the plastic sliding. Resistance against sliding on a contact plane depends on the degree of interlocking by neighboring particles. The resistance can be related to the packing void ratio e by

$$\tan\phi_p = \left(\frac{e_c}{e}\right)^m \tan\phi_\mu \qquad [9.21]$$

where m is a material constant and e_c corresponds to the critical void ratio for a given state of stress. For dense packing, e_c/e is greater than 1 and, therefore, the apparent inter-particle friction angle ϕ_p is greater than the internal friction angle ϕ_μ. When the packing structure dilates, the degree of interlocking and the apparent frictional angle are reduced. The result is a strain-softening phenomenon. For the loose packing, the apparent frictional angle ϕ_p, being smaller than the internal friction angle ϕ_μ, increases during the material contraction.

For this study, we selected a soil made of non-cohesive particles, typically a silt-sand-gravel mixture, with a grain size distribution susceptible to suffusion, according to the criteria proposed by Wan and Fell [WAN 04]. The material parameters were selected by using the correlations suggested by Biarez and Hicher

[BIA 94] relating the physical properties of a granular assembly to its mechanical properties. The maximum and minimum void ratios of a widely graded granular material are typically $e_{max} = 0.6$ and $e_{min} = 0.25$. We can, hereafter, derive the values of the two parameters corresponding to the position of the critical state in the *e-p'* plane defined by its slope $\lambda = 0.05$ and a given reference point; $p_{ref} = 0.01$ MPa for $e_{ref} = e_{max} = 0.6$. The friction angle at critical state ϕ_μ is considered equal to 32°. In the equation [9.21], the value of m is taken to equal 0.5, which is a typical value for this type of soil. The set of parameters for the selected soil is presented in Table 9.2.

e_{ref}	p_{ref} (MPa)	λ	ϕ_μ(°)	ϕ_0(°)	m
0.6	0.01	0.05	32	32	0.5

Table 9.2. *Model parameters for the selected soil*

Figure 9.17 presents a set of numerical results obtained with the set of parameters from Table 9.2 with different initial void ratios corresponding to density indexes I_D between 0 and 1 for an initial isotropic stress equal to 200 kPa. A reasonable simulation of the sand behavior can be obtained with a single set of model parameters, capturing both the contractive and dilative behaviors of the sand as well as the influence of this contractive or dilative behavior on the stress-strain curves and on the maximum strength. For large deformations, the curves corresponding to different initial void ratios converge toward an identical stress state and void ratio, in accordance with the definition of the critical state.

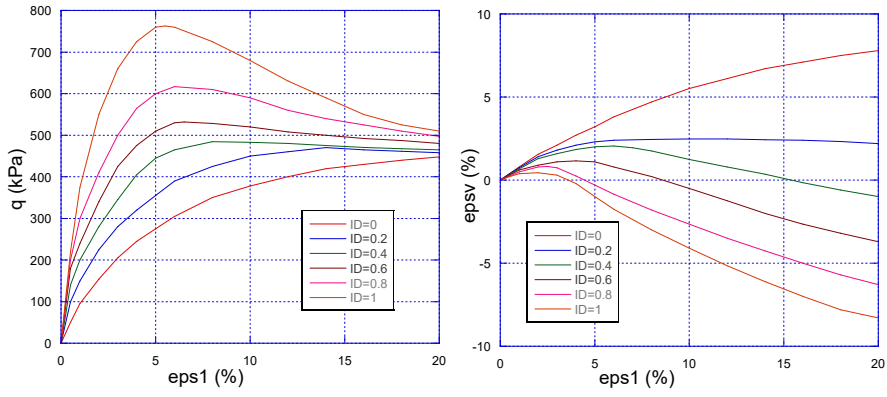

Figure 9.17. *Simulations of drained triaxial tests on the selected soil (p'0 = 200 kPa). For a color version of the figure, see www.iste.co.uk/millet/advances.zip*

Maximum strength is an increasing function of the initial density. Assuming a Mohr-Coulomb criterion, the plastic limits, a function of the initial density index, are plotted in the *p', q* plane, as well as the stress paths for the five drained triaxial tests (Figure 9.18). The slope of the maximum strength line increases when the density index increases.

The relationship between the relative slope increase expressed by the ratio η_{max}/η_c and the initial void ratio e is plotted in Figure 9.19; η_c being the stress ratio q/p' at critical state equal to 1.29 for the selected soil. For $I_D = 0$, the material is purely contractive and the maximum deviatoric stress state coincides with the critical state. When the density index increases, the stress-strain curves present a peak, the stress ratio at the peak is higher than η_c, after which the material softens and the stress ratio converges toward η_c at large strains. The evolution of η_{max}/η_c with e shows, at first, a slight increase as long as the material remains mainly contractive, before becoming more marked for higher values of I_D when the material becomes essentially dilative.

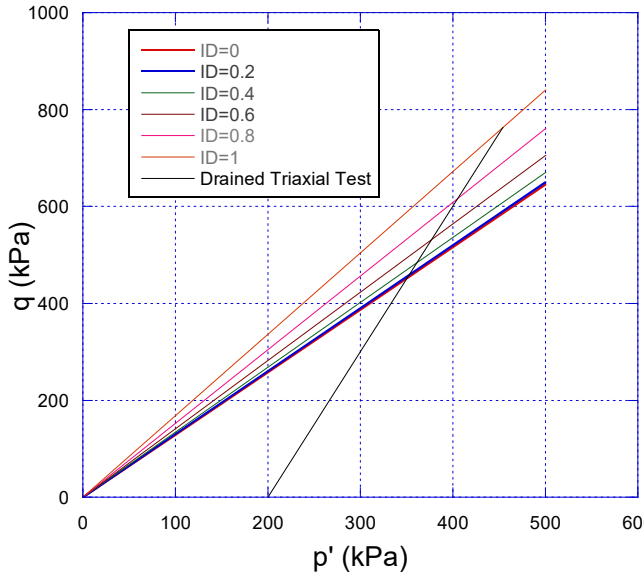

Figure 9.18. *Maximum strength envelopes for different initial densities. For a color version of the figure, see www.iste.co.uk/millet/advances.zip*

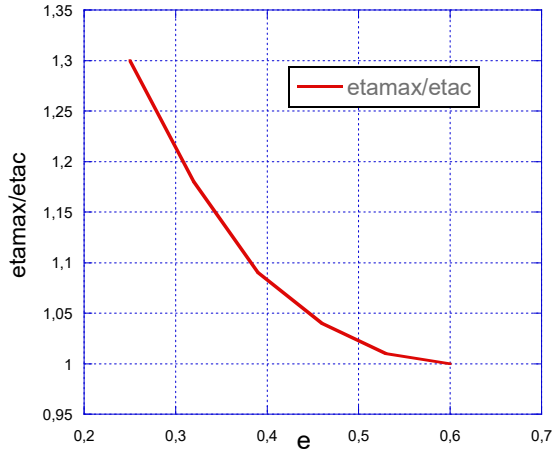

Figure 9.19. *Maximum strength ratio versus initial void ratio*

9.5.2.2. *Modeling the erosion process*

What could be the impact of removing a part of the solid fraction on the behavior of granular materials? The model cannot take into account the size of individual particles. Only the mean size value is considered as a model parameter. In this study, we will simply consider the removal of a given fraction *fe* of the solid particles defined as follows

$$fe = Wf / Ws \qquad [9.22]$$

where *Wf* is the weight of the extracted particles and *Ws* is the total solid weight. If we can assume that the particle density is the same for any particle size and that no deformation takes place during the extraction of solid particles, the total volume remains constant and the volume occupied by the extracted particles is replaced by the same volume of voids. Therefore, we can write:

$$(\Delta e)_{er} = \frac{fe\,(1+e_0)}{1-fe} \qquad [9.23]$$

where e_0 is the initial soil void ratio before the extraction process begins and $(\Delta e)_{er}$ is the void ratio due to the extraction process.

When the eroded fraction *fe* increases progressively, it creates a change in the void ratio. If the material is subjected to a constant state of external stresses, the evolution of the sliding resistance when the void ratio is changed creates a disequilibrium at each contact point leading to local sliding. All the local

displacements are then integrated to produce the macroscopic deformation of the soil specimen. This macroscopic deformation induces a volumetric change ε_v and, therefore, a change in the void ratio which is added to the void ratio change caused by particle removal:

$$(\Delta e)_{\text{total}} = (\Delta e)_{\text{er}} + \varepsilon_v(1+e) \qquad [9.24]$$

The void ratio is calculated at the end of each step which consists, at first, of imposing a change in void ratio corresponding to an incremental increase of the eroded fraction *fe* and then of calculating the induced deformations.

9.5.2.3. *Impact of erosion on soil behavior*

Typical results of the impact of solid particle extraction are presented in Figure 9.20. Several erosion tests were simulated at various stress levels. A dense sample with an initial void ratio $e_0 = 0.32$, corresponding to a density index $I_D = 0.8$, was selected for this study.

Each specimen is initially subjected to a triaxial loading up to a given state of stress and then to progressive particle removal while the external stresses are kept constant. All the specimens are isotropically consolidated up to $p' = 200$ kPa and then compressed up to a given stress levels $\eta = q/p'$ equal to 1.03, 1.35 and 1.42, corresponding to ratios η/η_c = 0.8, 1.05 and 1.1, respectively. The maximum strength of the material is equal to q = 616 kPa, corresponding to a stress ratio $\eta_{max} = q/p = 1.52$. One notices that the erosion induced deformations are larger when the stress ratio is higher. For low stress ratios, the strain amplitude remains limited to values lower than 1% when the eroded fraction increases up to 15%. Under these conditions, the soil can be said to remain stable and the damage induced within the earth structure is limited. For higher stress ratios, the deformation increases much faster and large deformations can occur for eroded fractions measuring more than 4% and 7% for the studied cases. The stress level above which large strains develop during the erosion process corresponds to the critical stress level η_c. The explanation for this result can be found in Figures 9.19 and 9.22 derived from Figure 9.21. The maximum strength envelope plotted in Figure 9.19 is dependent on the material density. When the density decreases due to particle extraction, the slope of the maximum strength envelope decreases down to η_c. If the stress ratio of the constant stress state during erosion is higher than η_c, the plastic limit converges toward the stress state and failure occurs. This is well illustrated by the plots in Figure 9.22. The plastic limit in the e, η_{max}/η_c plane is an ultimate state for the material, which cannot be exceeded. During particle extraction at constant η_{max}/η_c, the state point moves toward this limit and specimen failure develops when this state point reaches the plastic limit. For $\eta < \eta_c$, this limit cannot be attained and the specimen remains stable even for high *fe* values.

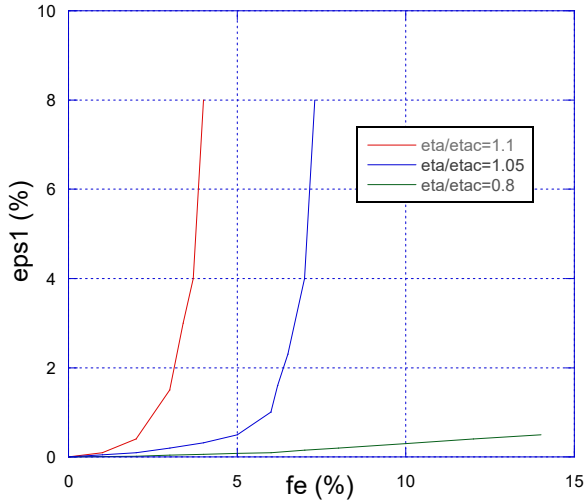

Figure 9.20. *Evolution of axial strain during erosion tests at constant deviatoric stress ratios. For a color version of the figure, see www.iste.co.uk/millet/advances.zip*

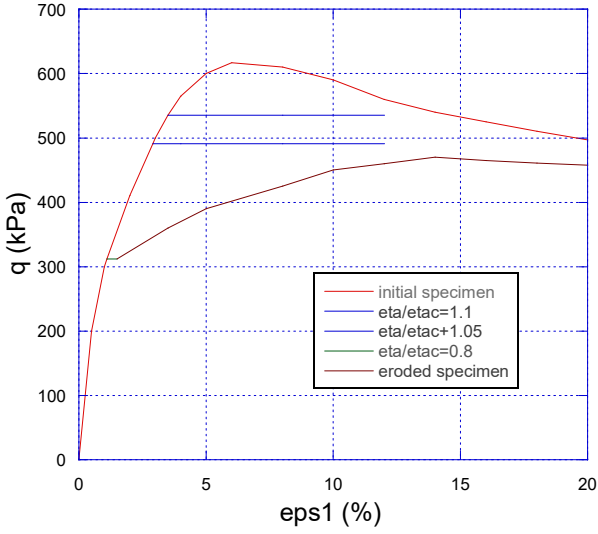

Figure 9.21. *Stress-strain relationship before, during and after erosion. For a color version of the figure, see www.iste.co.uk/millet/advances.zip*

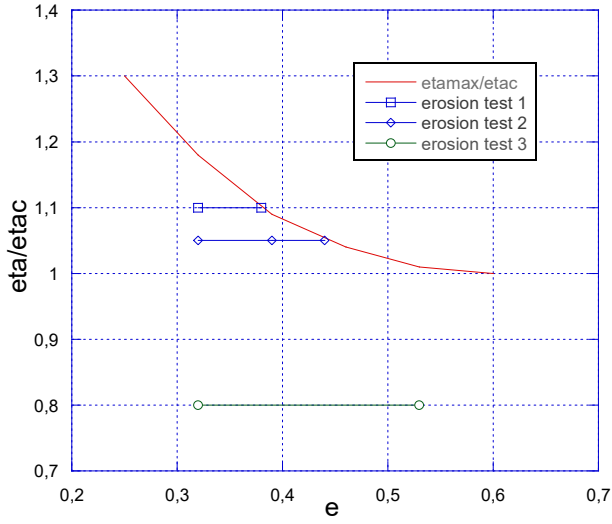

Figure 9.22. *Evolution of the mechanical state of the material during erosion. For a color version of the figure, see www.iste.co.uk/millet/advances.zip*

The specimens which did not experience significant deformation during erosion are, however, subjected to density changes due to the removal of the solid fraction *fe*. In accordance with the increase of porosity induced by particle removals, the degraded specimen behaves as does a loose material with significant contraction and monotonic increase of the stress ratio (see Figure 9.21).

9.5.3. *Comparison between numerical results from DEM and micromechanical model*

Even if these two particle removal procedures do not correspond to any realistic erosion process, the description of its consequences on the granular assembly stability appears strikingly similar. It would, therefore, be interesting to see if we can obtain comparative results by simulating with the micromechanical model the numerical tests performed by DEM.

In this study, the normal stiffness and the ratio between tangential and normal stiffness are taken to be equal to the values considered by the DEM approach. The parameters of the plastic part of the contact law are given in Table 9.3. Parameters determining the critical state line of the DEM simulations are, as well as the value of *m*, calibrated by curve fitting using the test results shown in Figure 9.6.

e_{ref}	p_{ref} (MPa)	λ	ϕ_μ(°)	ϕ_0(°)	m
0.78	0.01	0.05	19	19	3

Table 9.3. *Model parameters for the DEM assembly of spheres*

Figure 9.23 presents the simulations done by the micromechanical model. Several erosion tests were simulated at various stress levels. The results demonstrate that, for elevated deviatoric stresses, the model gives similar results as the ones obtained by DEM. Progressive deformations develop within the specimens during the erosion process. For high stress levels, the axial strains increase rapidly and lead to specimen failure (Figure 9.24). The strain path is linked to the stress ratio. The test at a stress ratio equal to η^{cs}= 0.72, corresponding to the value of *q/p'* at critical state obtained from the drained triaxial test, deforms roughly at constant volume. At higher stress ratios, the volume increases during erosion, whereas at smaller stress ratios it decreases. This behavior is in complete agreement with the DEM simulations, as can be seen in Figure 9.16.

For smaller deviatoric stresses, however, it seems that the DEM simulations produce larger deformations during erosion than those produced by the microstructural model. Indeed, rather large values of the eroded fraction *fe* are required in order to obtain a significant straining of the specimens (Figure 9.24).

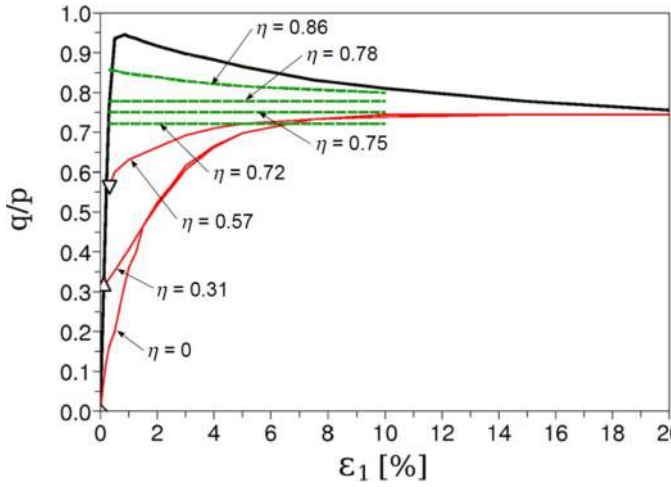

Figure 9.23. *Simulations of particle extraction by the microstructural model. For a color version of the figure, see www.iste.co.uk/millet/advances.zip*

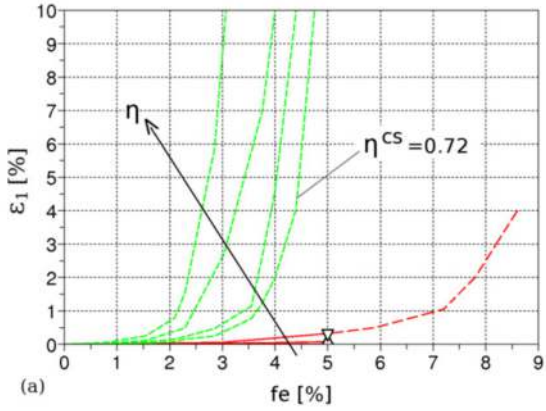

Figure 9.24. *Evolution of the vertical deformation during erosion at different stress levels: micromechanical model simulations. For a color version of the figure, see www.iste.co.uk/millet/advances.zip*

As in the DEM approach, in accordance with the increase of porosity induced by particle removals, degraded specimens behave like a loose material with significant contraction and monotonic increase of the stress ratio. In particular, the internal friction angle decreases from 24° for the intact medium, to 20° for the degraded ones, which corroborates well with the shear strength reduction given by DEM simulations.

9.5.4. *Conclusion*

Based on two numerical approaches, this study examined the influence of removing a part of the solid fraction on specific soil properties. The material was selected in such a way as to limit the computational cost concerning the DEM approach (by limiting the range of the size of particles). However the grain size distribution of this material is not typical of the soils likely to develop internal erosion; thus, the results obtained should be confirmed for such soils. The parameter values typical for this kind of material were assumed by using the correlations between micro and macro properties of granular materials. As for the micromechanical model, the progressive removal of the solid fraction leads to a decrease of the sliding resistance of each inter-particle contact, which creates a disequilibrium between the external applied loading and the internal contact forces. As a consequence, local slidings occur which lead to macroscopic deformations of the soil specimen. The amplitude of the induced deformations depends both on the amount of particles removed and the level of stress applied. At elevated stress levels, large deformations can develop when the removed fraction increases. The result in this case is the failure of the material because the plastic limit evolves with the

density decrease during erosion and falls into contact with the stress state of the material.

9.6. General conclusion

One of the main qualitative distinctions between internal erosion processes comes from the important role played by self-filtration in the development of erosion. On one hand, in the case of interface erosion, self-filtration generally cannot occur and the hydraulic loading of the soil can be represented by the hydraulic shear stress or the fluid flow power. On the other hand, in the case of suffusion, self-filtration can develop and may influence the progression of erosion, depending on its relative importance with respect to particle detachment. Then, it seems necessary to take into account not just the instantaneous hydraulic loading but the whole hydraulic loading history through the interstitial fluid flow energy cumulated over the hydraulic loading duration in order to describe the development of suffusion.

Initiation of suffusion does not lead directly to significant deformations of the soil subjected to an external loading (which could be its own weight). However, its development over a longer period can evolve toward a strong erosion and can affect the soil shear strength. At the scale of a hydraulic embankment, suffusion development could even cause its complete failure. Therefore, for risk management concerning water-retaining earth structures, it is very helpful to characterize the effects induced by suffusion development on the mechanical behavior of soils.

One should keep in mind that most of the conclusions drawn in this chapter result from studies realized for specific grading curves, with respect to their shape and their extent. Generalizing these findings still requires further analyses on different kinds of soils in order to extend knowledge of soil sensitivity to erosion, on the one hand, and the consequences of its evolution on the mechanical behavior of the eroded soil, on the other hand.

9.7. Bibliography

[BAG 56] BAGNOLD R., "The flow of cohesionless grains in fluids", *Philosophical Transactions of the Royal Society of London, Series A, Mathematical and Physical Sciences*, vol. 249, pp. 235–297, 1956.

[BAG 80] BAGNOLD R., "An empirical correlation of bedload transport rates in flumes and natural rivers", *Proceedings of the Royal Society of London A Mathematical, Physical and Engineering Sciences*, vol. 372, pp. 453–473, 1980.

[BEL 74] BELTAOS S., RAJARATNAM. N., "Impinging circular turbulent jets", *Journal of the Hydraulics Division*, vol. 100 (HY10), pp. 1313–1328, 1974.

[BEN 08] BENDAHMANE F., MAROT D., ALEXIS A., "Parametric study of suffusion and backward erosion", *Journal of Geotechnical and Geoenvironmental Engineering,* vol. 134, no. 1, pp. 57–67, 2008.

[BIA 94] BIAREZ J., HICHER P.-Y., *Elementary Mechanics of Soil Behaviour*, Balkema, Rotterdam, 1994.

[BON 08] BONELLI S., BRIVOIS O., "The scaling law in the hole erosion test with a constant pressure drop", *International Journal for Numerical and Analytical Methods in Geomechanics*, vol. 32, no. 13, pp. 1573–1595, 2008.

[BON 11] BONELLI S., MAROT D., "Micromechanical modeling of internal erosion", *European Journal of Environmental and Civil Engineering*, vol. 15, pp. 1207–1224, 2011.

[CHA 05] CHANG C.S., HICHER P.Y., "An elastoplastic model for granular materials with microstructural consideration", *International Journal of Solids and Structures*, vol. 42, no.14, pp. 4258–4277, 2005.

[CHA 11] CHANG D.S., ZHANG L.M., "A Stress-controlled erosion apparatus for studying internal erosion in soils", *Geotechnical Testing Journal*, vol. 34, no. 6, pp. 579–589, 2011.

[FEL 07] FELL R., FRY J.J. (eds), *Internal Erosion of Dams and Their Foundations*, Taylor & Francis, Abingdon, 2007.

[FEL 13] FELL R., FRY J.J., "State of the Art on the Likelihood of Internal Erosion of Dams and Levees by Means of Testing", in BONELLI S. (ed.), *Erosion in Geomechanics Applied to Dams and Levees*, ISTE Ltd., London and John Wiley Sons, New York, 2013.

[FER 98] FERRO V., "Evaluating overland flow sediment transport capacity", *Hydrological Processes*, vol. 12, pp. 1895–1910, 1998.

[FOS 00] FOSTER M., FELL R., SPANNAGLE M., "The statistics of embankment dam failures and accidents", *Canadian Geotechnical Journal*, vol. 37, pp. 1000–1024, 2000.

[FRY 12] FRY J.J., VOGEL A., ROYET P. *et al.*, "Dam failures by erosion: lessons from ERINOH data bases", *Proceedings of the 6th International Conference on Scour and Erosion (ICSE-6)*, 27–31 August, Paris, France, pp. 273–280, 2012.

[GAR 10] GARNER S.J., FANNIN R.J., "Understanding internal erosion: a decade of research following a sinkhole event", *The International Journal on Hydropower & Dams*, vol. 17, pp. 93–98, 2010.

[GOV 92] GOVERS G., "Evaluation of transporting capacity formulae for overland flow", in PARSONS A., ABRAHAMS A. (eds), *Overland Flow*, UCL Press, London, 1992.

[HAN 04] HANSON G.J., COOK K.R., "Apparatus, test procedures, and analytical methods to measure soil erodibility in-situ", *Applied Engineering in Agriculture*, vol. 20, no. 4, pp. 455–462, 2004.

[HAN 01] HANSON G.J., SIMON A., "Erodibility of cohesive streambeds in the loess area of the midwestern U.S.A.", *Hydrological Processes*, vol. 15, no. 1, pp. 23–38, 2001.

[HIC 13] HICHER P.Y., "Modelling the Impact of Particle Removal on Granular Material Behaviour", *Géotechnique*, vol. 63, no. 2, pp. 118–128, 2013.

[KE 12] KE L., TAKAHASHI A., "Strength reduction of cohesionless soil due to internal erosion induced by one dimensional upward seepage flow", *Soils and Foundations*, vol. 52, pp. 698–711, 2012.

[KEN 85] KENNEY T.C., LAU D., "Internal stability of granular filters", *Canadian Geotechnical Journal*, vol. 22, pp. 215–225, 1985.

[LAF 89] LAFLEUR J., MLYNAREK J., ROLLIN A.L., "Filtration of broadly graded cohesionless soils", *Journal of Geotechnical Engineering*, vol. 115, no. 12, pp. 1747–1768, 1989.

[LOM 13] LOMINÉ F., SCHOLTÈS L., SIBILLE L. *et al.*, "Modelling of fluid-solid interaction in granular media with coupled LB/DE methods: application to piping erosion", *International Journal for Numerical and Analytical Methods in Geomechanics*, vol. 37, pp. 577–596, 2013.

[LOW 89] LOW H., "Effect of sediment density on bed-load transport", *Journal of Hydraulic Engineering*, vol. 115, pp. 124–138, 1989.

[MAR 09] MAROT D., BENDAHMANE F., ROSQUOËT F. *et al.*, "Internal flow effects on isotropic confined sand-clay mixtures", *Soil & Sediment Contamination, an International Journal*, vol. 18, no. 3, pp. 294–306, 2009.

[MAR 11a] MAROT D., REGAZZONI P.L., WAHL T., "Energy based method for providing soil surface erodibility rankings", *Journal of Geotechnical and Geoenvironmental Engineering (ASCE)*, vol. 137, no. 12, pp. 1290–1294, 2011.

[MAR 11b] MAROT D., BENDAHMANE F., KONRAD J.M., "Multichannel optical sensor to quantify particle stability under seepage flow", *Canadian Geotechnical Journal*, vol. 48, pp. 1772–1787, 2011.

[MAR 12a] MAROT D., LE V., GARNIER J. *et al.*, "Study of scale effect in an internal erosion mechanism: centrifuge model and energy analysis", *European Journal of Environmental and Civil Engineering*, vol. 16, pp. 1–19, 2012.

[MAR 12b] MAROT D., BENDAHMANE F., NGUYEN H.H., "Influence of angularity of coarse fraction grains on internal erosion process", *La Houille Blanche, International Water Journal*, vol. 6, pp. 47–53, 2012.

[MOF 06] MOFFAT R., FANNIN R.J., "A large permeameter for study of internal stability in cohesionless soils", *Geotechnical Testing Journal*, vol. 29, no. 4, pp. 273–279, 2006.

[MOF 11a] MOFFAT R., FANNIN R.J., "A hydromechanical relation governing internal stability of cohesionless soil", *Canadian Geotechnical Journal*, vol. 48, no. 3, pp. 413–424, 2011.

[MOF 11b] MOFFAT R., FANNIN R.J., GARNER S.J., "Spatial and temporal progression of internal erosion in cohesionless soil", *Canadian Geotechnical Journal*, vol. 48, no. 3, pp. 399–412, 2011.

[MOR 97] MOREAU J.J., "Numerical investigation of shear zones in granular materials", in WOLF D.E., GRASSBERGER P. (eds), *Friction, Arching, Contact Dynamics*, World Scientific, Singapore, 1997.

[MUI 10] MUIR WOOD D., MAEDA K., NUKUDANI E., "Modelling mechanical consequences of erosion", *Géotechnique*, vol. 60, no. 6, pp. 447–457, 2010.

[NGU 12] NGUYEN H.H., MAROT D., BENDAHMANE F., "Erodibility characterisation for suffusion process in cohesive soil by two types of hydraulic loading", *La Houille Blanche, International Water Journal*, vol. 6, pp. 54–60, 2012.

[PER 07] PERZLMAIER S., "Hydraulic criteria for internal erosion in cohesionless soil", in FELL R., FRY J.J. (eds), *Internal Erosion of Dams and Their Foundations*, Taylor & Francis, Abingdon, pp. 179–190, 2007.

[RED 00] REDDI L.N., LEE I., BONALA M.V.S., "Comparison of internal and surface erosion using flow pump test on a sand-kaolinite mixture", *Geotechnical Testing Journal*, vol. 23, no. 1, pp. 116–122, 2000.

[REG 11] REGAZZONI P.-L., MAROT D., "Investigation of interface erosion rate by Jet Erosion Test and statistical analysis", *European Journal of Environmental and Civil Engineering*, vol. 15, no. 8, pp. 1167–1185, 2011.

[REG 13] REGAZZONI P.-L., MAROT D., "A comparative analysis of interface erosion tests", *Natural Hazards*, vol. 67, pp. 937–950, 2013.

[SAI 11] SAIL Y., MAROT D., SIBILLE L. *et al.*, "Suffusion tests on cohesionless granular matter", *European Journal of Environmental and Civil Engineering*, vol. 15, no. 5, pp. 799–817, 2011.

[SCH 10] SCHOLTÈS L., HICHER P.Y., SIBILLE L., "Multiscale approaches to describe mechanical responses induced by particle removal in granular materials", *Comptes Rendus Mécanique*, vol. 338, nos. 10–11, pp. 627–638, 2010.

[SIB 15a] SIBILLE L., MAROT D., SAIL Y., "A description of internal erosion by suffusion and induced settlements on cohesionless granular matter", *Acta Geotechnica*, vol. 10, no. 6, pp. 735–748, 2015.

[SIB 15b] SIBILLE L., LOMINÉ L., POULLAIN P. *et al.*, "Internal erosion in granular media: direct numerical simulations and energy interpretation", *Hydrological Processes*, vol. 29, no. 9, pp. 2149–2163, 2015.

[SKE 94] SKEMPTON A.W., BROGAN J.M., "Experiments on piping in sandy gravels", *Géotechnique*, vol. 44, no. 3, pp. 440–460, 1994.

[VOI 08] VOIVRET C., Texture et comportement des matériaux granulaires à grande polydispersité, PhD Thesis, Montpellier 2 University, 2008.

[WAN 04] WAN C.F., FELL R., "Investigation of rate of erosion of soils in embankment dams", *Journal of Geotechnical and Geoenvironmental Engineering*, vol. 130, no. 4, pp. 373–380, 2004.

[WAN 08] WAN C.F., FELL R., "Assessing the potential of internal instability and suffusion in embankment dams and their foundations", *Journal of Geotechnical and Geoenvironmental Engineering,* vol. 134, no. 3, pp. 401–407, 2008.

[WHI 99] WHITE F.M., *Fluid Mechanics*, 4th ed., McGraw Hill, New York, 1999.